

AnatomiX, an Anatomy-Aware Grounded Multimodal Large Language Model for Chest X-Ray Interpretation

Anees Ur Rehman Hashmi
 Hasso Plattner Institute
 Potsdam, Germany
 anees.hashmi@hpi.de

Numan Saeed
 MBZUAI
 Abu Dhabi, UAE
 numan.saeed@mbzuai.ac.ae

Christoph Lippert
 Hasso Plattner Institute
 Potsdam, Germany
 christoph.lippert@hpi.de

Abstract

Multimodal medical large language models have shown impressive progress in chest X-ray interpretation but continue to face challenges in spatial reasoning and anatomical understanding. Although existing grounding techniques improve overall performance, they often fail to establish a true anatomical correspondence, resulting in incorrect anatomical understanding in the medical domain. To address this gap, we introduce AnatomiX, a multitask multimodal large language model explicitly designed for anatomically grounded chest X-ray interpretation. Inspired by the radiological workflow, AnatomiX adopts a two stage approach: first, it identifies anatomical structures and extracts their features, and then leverages a large language model to perform diverse downstream tasks such as phrase grounding, report generation, visual question answering, and image understanding. Extensive experiments across multiple benchmarks demonstrate that AnatomiX achieves superior anatomical reasoning and delivers over 25% improvement in performance on anatomy grounding, phrase grounding, grounded diagnosis and grounded captioning tasks compared to existing approaches. Code and pretrained model are available at github.com/aneesurhashmi/anatomix

1. Introduction

Multimodal Large Language Models (MLLMs) are being increasingly applied in the natural and medical imaging domain to perform multiple tasks using a single model [36]. These models typically consist of an image encoder and a Large Language Model (LLM), and utilize the pretrained LLM’s strengths by passing image embeddings along with a text prompt into the LLM to perform downstream tasks [20]. The pretrained LLMs are generally trained on very large text corpora and therefore demonstrate strong text generation capabilities, making them suitable for a diverse set of downstream tasks after supervised fine-tuning and

instruction tuning [1, 24]. However, owing partly to their autoregressive design and the challenges of merging vision and language modalities, MLLMs still struggle with fine-grained spatial understanding, for instance, when reasoning about positions of multiple objects or their relative spatial relations in a scene [21, 34].

This issue of MLLMs has previously been addressed by introducing object grounding, which aligns the text concepts with the objects in the image [28, 33]. Grounding in MLLMs is usually achieved by training the model on a dataset containing the names or descriptions of local objects in the image plus their bounding boxes or segmentation masks as spatial markers. This in turn improves the reasoning abilities of MLLMs with better concept understanding, making them applicable in the medical domain, where spatial reasoning is essential. In particular, chest X-ray (CXR) interpretation greatly benefits from such multimodal reasoning, as accurate localization and semantic alignment between textual findings and radiographic regions are crucial for diagnosis. MLLMs like ViviMed [23], ChexAgent [7], RadVLM [10] and MAIRA-2 [4] show that grounding via special tokens yields consistent performance gains on CXR image tasks.

Although incorporating grounding through additional tokens has improved MLLMs’ spatial reasoning, it remains insufficient for the fine-grained localization and differentiation required in medical imaging, where anatomically distinct regions often exhibit highly similar visual textures and appearances [34]. As illustrated in Fig. 1, current state-of-the-art (SOTA) MLLM fails to correctly localize lesions or identify the correct anatomical objects when presented with flipped images - where the left and right sides are switched. These models may perform well on standard orientations but fail when spatial cues are inverted, revealing that they overly rely on spatial correlations rather than recognition of anatomical structures, exposing a critical gap between visual grounding and medical comprehension.

This weak anatomical understanding in current medical MLLMs is likely due to their single-step visual grounding

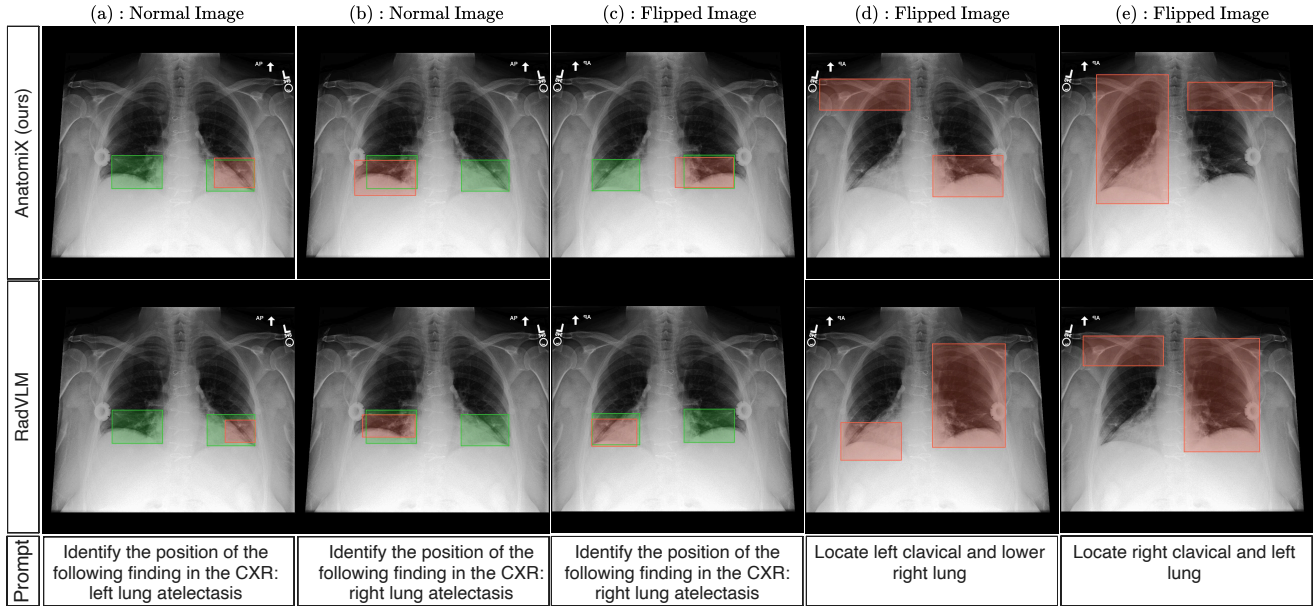


Figure 1. Comparison between AnatomiX and RadVLM [10] in anatomy understanding. (a) and (b) show both models predicting the disease on the correct side (color scheme: red for model’s output, green for all ground truth locations). (c), (d) and (e) show models’ outputs for the same image flipped on the vertical axis (left \leftrightarrow right), where RadVLM completely fails to recognize the correct anatomical object, while AnatomiX successfully recognizes the correct anatomies, showcasing high anatomical understanding

process. Specifically, these models must implicitly detect the correct anatomical objects within an image before performing the downstream task. This one-step process differs fundamentally from the workflow of radiologists, who iteratively identify, localize, and evaluate each anatomical structure before drawing diagnostic conclusions. To address this issue, we introduce *AnatomiX*, an anatomy-aware grounded MLLM for chest X-Ray interpretation. AnatomiX uses a two stage process to first identify different thoracic anatomical objects (organs) before performing the task; thereby, showing a high anatomical understanding compared to existing CXR grounding MLLMs as shown in Fig. 1. Our proposed model significantly outperforms SOTA models on four grounding tasks and shows SOTA or on-par performance on report generation, VQA and image understanding tasks. Extensive experiments on a large collection of datasets show the high reasoning and anatomical understanding capabilities of AnatomiX. In summary, our work makes the following contributions:

- We introduce *AnatomiX*, an anatomy-aware grounded multimodal large language model for chest X-Ray interpretation.
- AnatomiX achieves SOTA performance on a CXR related grounding task, while maintaining on-par or better performance on report-generation, VQA and image understanding tasks.
- We demonstrate the robustness of AnatomiX across different datasets and perform ablations to validate the con-

tribution of each component.

2. Related Work

Early adaptations of MLLMs to radiology primarily involve fine-tuning general-domain models on medical datasets. LLaVA-Med [16] and RadVLM [10] extend LLaVA [20] for multi-task CXR benchmarks, improving both report generation and VQA. Several works introduce explicit grounding for CXR tasks: ViviMed [23] and MedRG [38] pair the Segment-Anything model [15] with an LLM for detection and segmentation, while MAIRA-2 [4] enables grounded report generation through additional tokens. Similarly, RadVLM [10] constructs a large instruction dataset for diverse CXR tasks, whereas CheXagent [7] applies contrastive learning and instruction tuning to enhance phrase grounding and CXR report generation. Radialog [27] supports multi-turn CXR conversations, and MedGemma [30] adapts Gemma-3 for general purpose medical tasks by fine-tuning on large-scale medical datasets. More recently, AOR [17] introduced region level information in LLM for CXR interpretation; however, this model is not yet publicly available for testing and comparison.

Most prior efforts adapt general-domain MLLMs rather than developing domain-specific architectures. CheX [25] advances toward anatomy-aware modeling by incorporating anatomical objects from CXR reports but lacks prompt-based interaction and generative flexibility. Overall, ex-

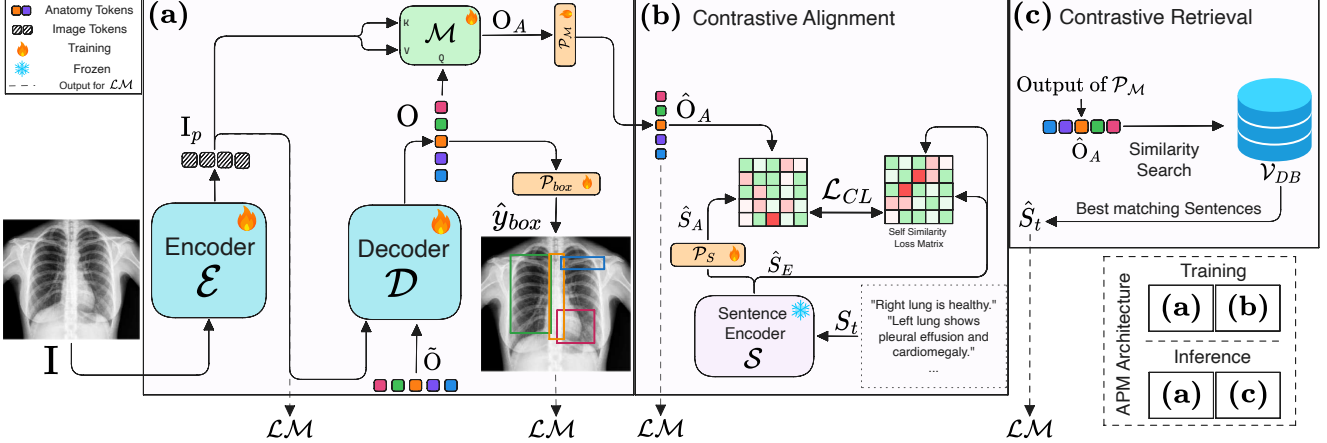


Figure 2. Anatomy Perception Module (APM) architecture (a): The encoder \mathcal{E} outputs image embedding I_p , while the decoder \mathcal{D} and feature extraction module \mathcal{M} output object bounding boxes \hat{y}_{box} , and anatomical object tokens \hat{O}_A , respectively. Different colors in \hat{O} , O and \hat{O}_A represent specific anatomical objects. (b) shows the contrastive alignment using frozen sentence encoder \mathcal{S} and self-similarity loss. (c): The vector database (\mathcal{V}_{DB}) contains the text sentences and embeddings used for contrastive retrieval. (Bottom right): APM uses (a) and (b) during training, and replaces (b) with (c) during inference. The \mathcal{P} represent different FC projectors described in section 3.1.

isting CXR MLLMs rely on instruction tuning and large-scale radiology datasets, achieving strong benchmark performance yet showing limited reasoning and anatomical understanding [34]. In contrast, our approach introduces a two-stage anatomy-aware pipeline that explicitly models thoracic structures before performing downstream tasks.

3. Methodology

This section describes the architecture of AnatomiX, which comprises two primary components: The Anatomy Perception Module and a large language model outlined below.

3.1. Anatomy Perception Module

Given an input CXR image I , the objective of the Anatomy Perception Module (APM) is to extract a global image representation along with fine-grained features corresponding to N thoracic anatomical objects. The resulting representations are subsequently used by an LLM for downstream tasks. The APM adopts a multi-task learning framework that jointly learns global image features, object localization through bounding boxes, and their detailed anatomical representations, while also retrieving textual descriptions associated with each anatomical object. Fig. 2 shows the detailed architecture of the APM, which consists of an image encoder (\mathcal{E}), a decoder (\mathcal{D}), a feature extraction module (\mathcal{M}) and a sentence encoder (\mathcal{S}). The details of each component are given below.

Image Encoder \mathcal{E} and Decoder \mathcal{D} :

The input image I is first encoded by the image encoder \mathcal{E} producing the image representation $I_p \in \mathbb{R}^{P \times d}$ which consists of P patch embedding vectors of dimension d . To

gether, these form a global representation of the image. These embeddings serve as the shared representation of visual information for subsequent modules. Specifically, I_p is provided both to the feature extractor \mathcal{M} , which focuses on semantic anatomy cues, and to the decoder \mathcal{D} , which is inspired by DETR [6]. The decoder processes I_p jointly with N learnable object tokens $\hat{O} = [\hat{o}^1, \dots, \hat{o}^N]$, using transformer blocks to perform cross-attention between tokens and image patches. Through this interaction, each object token learns to attend to relevant anatomical regions, resulting in updated token embeddings O that encode the localization of the N anatomical objects.

$$O = \mathcal{D}(I_p, \hat{O}) \quad (1)$$

where $O \in \mathbb{R}^{N \times d} = [o^1, \dots, o^N; o^i \in \mathbb{R}^d]$

The object tokens O are projected using a fully connected (FC) projector \mathcal{P}_{box} to predict a bounding box for each anatomical object ($\hat{y}_{box} = \mathcal{P}_{box}(O)$), as illustrated in Fig. 2. Unlike DETR [6], O is not permutation invariant, which means that each element of O corresponds to exactly one predefined anatomical object. This design enables each token o^i to focus on and extract information related to the i^{th} anatomical object from I_p . To effectively learn the \hat{y}_{box} localization, we use a combination of L1 and intersection over union (IoU) losses as shown in eq. 2 and 3.

$$\mathcal{L}_{IoU}(\hat{y}_{box}, y_{box}) = 1 - \frac{|\hat{y}_{box} \cap y_{box}|}{|\hat{y}_{box} \cup y_{box}|} \quad (2)$$

$$\mathcal{L}_{box} = \lambda_1(|\hat{y}_{box} - y_{box}|) + \lambda_2 \mathcal{L}_{IoU}(\hat{y}_{box}, y_{box}) \quad (3)$$

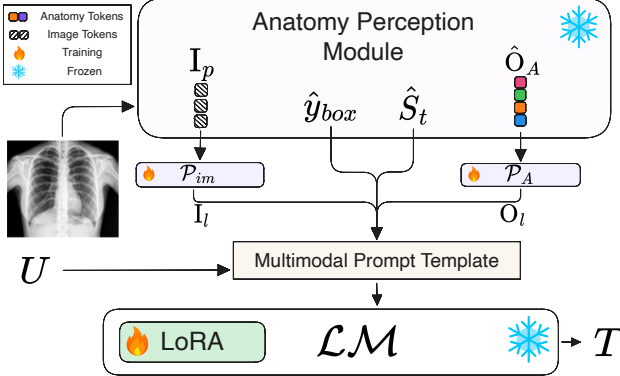


Figure 3. Overall architecture of Anatomix. The outputs of the APM and the user prompt U are added to a structured multimodal prompt template before being passed to the \mathcal{LM} , which generates the response T . \mathcal{P}_{im} and \mathcal{P}_A represent FC projectors as described in section 3.2.

where y_{box} represents ground truth bounded boxes, $\lambda_1 = 5$ and $\lambda_2 = 2$ are the weightings of the L1 Loss and the \mathcal{L}_{IoU} Loss, respectively, set to the default values used in DETR.

Feature Extraction Module \mathcal{M} :

In addition to predictions of the bounding boxes in the decoder output, we leverage the spatial information encoded in O to extract fine-grained representations of each anatomical object through the feature extraction module \mathcal{M} . Within \mathcal{M} , cross-attention is computed between O and image patches I_p as shown in eq. 4, where the anatomical object tokens O serve as queries (Q), and the image embedding I_p provides the keys (K) and values (V). Conceptually, \mathcal{M} can be viewed as an extension of the decoder \mathcal{D} , where the image representation I_p is re-included via a skip connection.

$$O_A = \mathcal{M}(Q, K, V) = \text{Softmax} \left(\frac{QK^T}{\sqrt{d}} \right) V, \quad (4)$$

where $Q = OW_Q$ is the query matrix, $K = I_p W_K$ is the key matrix and $V = I_p W_V$ is the value matrix.

The output O_A represent localized image features for the anatomical objects at the corresponding positions specified by the predicted bounding boxes \hat{y}_{box} . Subsequently, these features are projected to a lower-dimensional space ($d \rightarrow s$) using the projection module \mathcal{P}_M as: $\hat{O}_A = \mathcal{P}_M(O_A)$, which yields $\hat{O}_A \in \mathbb{R}^{N \times s}$.

Contrastive Alignment with \mathcal{S} :

During APM training, we perform localized contrastive alignment (Fig. 2-b) between each anatomical feature token $\hat{o}_A^i \in \hat{O}_A$ and its corresponding textual description $s^i \in S_t$,

where s^i specifies the radiological findings in the associated anatomical region (e.g. *Right Lung shows pneumonia, pleural effusion and atelectasis.*). Since \hat{O}_A encodes fine-grained visual representations of N anatomical objects derived from the image embedding I_p , aligning these tokens with the corresponding text sentence embeddings enables the model to establish correspondences between visual and semantic representations. This alignment ensures that the visual tokens capture each anatomical region's spatial and structural properties while linking them to clinically relevant textual concepts. The textual descriptions S_t are first encoded using the frozen sentence encoder \mathcal{S} (Biomed-BERT [11]) to obtain embeddings $\hat{S}_E \in \mathbb{R}^{N \times 768}$, which are then projected to a lower-dimensional space ($768 \rightarrow s$) using a fully connected projector \mathcal{P}_S for efficient contrastive learning.

$$\hat{S}_E = \mathcal{S}(S_t) \quad (5)$$

$$\hat{S}_A = \mathcal{P}_S(\hat{S}_E) \quad (6)$$

where $\hat{S}_A \in \mathbb{R}^{N \times s}$ represents projected text embeddings.

Radiological findings across thoracic anatomical objects often overlap or appear together, making it uncommon for an image to contain a finding in only one region. In such cases, using standard CLIP-style contrastive loss [29] can introduce many false negatives, as it assumes only one correct (positive) text-image pair per sample. To overcome this, we employ a soft contrastive loss that allows multiple degrees of similarity across anatomical regions. Specifically, we introduce a self-similarity matrix S_{self} (eq. 7), which permits non-zero similarity values for off-diagonal entries, reflecting the natural co-occurrence of anatomical observations (see the supplementary material section S1 for details). We optimize this alignment using Kullback–Leibler (KL) divergence as shown in eq. 8, which measures distributional differences instead of enforcing discrete class boundaries [13]. This makes it well-suited for overlapping or correlated anatomical feature representations and preserving partial similarities among different anatomical objects' features.

$$S_{self} = \hat{S}_E \hat{S}_E^T \quad (7)$$

$$\mathcal{L}_{CL}(\hat{S}_A, S_{self}) = \sum_i \hat{S}_A(i) \log \frac{\hat{S}_A(i)}{S_{self}(i)} \quad (8)$$

where $S_{self} \in \mathbb{R}^{N \times N}$

Finally, we train APM end-to-end using a combination of bounding box prediction and contrastive alignment losses.

$$\mathcal{L}_{APM} = \mathcal{L}_{box} + \mathcal{L}_{CL} \quad (9)$$

Contrastive Retrieval with \mathcal{V}_{DB} :

Since the textual descriptions S_t associated with anatomical objects are available only during APM training, we replace the sentence encoder \mathcal{S} with a compact vector database \mathcal{V}_{DB} during inference as shown in Fig. 2-(c). This database stores all unique textual sentences corresponding to each of the N anatomical regions, along with their precomputed embeddings. At inference time, each anatomical object token in $\hat{\mathcal{O}}_A$ is compared against the sentence embeddings in \mathcal{V}_{DB} to retrieve the most semantically similar sentence \hat{S}_t for that anatomical region as $\hat{S}_t = \mathcal{V}_{DB}(\hat{\mathcal{O}}_A)$. The retrieved sentences are then passed to LLM, along with the anatomical object tokens $\hat{\mathcal{O}}_A$, the predicted bounding boxes \hat{y}_{box} , and the image embeddings I_p . Additional implementation details of \mathcal{V}_{DB} are provided in the supplementary material section S2.

3.2. Large Language Model

Given the outputs of APM — image embeddings I_p , predicted locations of N anatomical objects \hat{y}_{box} and their corresponding features $\hat{\mathcal{O}}_A$ and retrieved text descriptions \hat{S}_t — and the user prompt U , the large language model \mathcal{LM} generates a textual response T performing the task specified in U . To achieve this, we construct a multimodal prompt template (shown in supplementary Fig. S1) that integrates the fine grained anatomical and textual information extracted in APM, and passes it to \mathcal{LM} . Fig. 3 shows the overall architecture of Anatomix. Firstly, to align the embedding spaces of APM and \mathcal{LM} , we project both the image embedding I_p and anatomical object tokens embedding $\hat{\mathcal{O}}_A$ into \mathcal{LM} 's embedding space using FC projectors. Specifically, \mathcal{P}_{im} ($d \rightarrow l$) maps the image embedding to $I_l = \mathcal{P}_{im}(I_p)$, where $I_l \in \mathbb{R}^{P \times l}$, and \mathcal{P}_A ($s \rightarrow l$) maps the anatomical object token embedding to $O_l = \mathcal{P}_A(\hat{\mathcal{O}}_A)$, where $O_l \in \mathbb{R}^{N \times l}$.

The language model \mathcal{LM} is based on MedGemma-4b-it [30] LLM architecture (excluding vision encoder). To enable anatomy aware reasoning, we extend the model's vocabulary by introducing N special tokens for anatomical objects ($\langle obj_i \rangle$ for $i \in [0, N]$) and four additional tokens for spatial grounding ($\langle box \rangle$, $\langle /box \rangle$, $\langle ref \rangle$, and $\langle /ref \rangle$). Each $\langle obj_i \rangle$ token corresponds to the feature representation of the i^{th} anatomical object, o_l^i , where $O_l = [o_l^1, \dots, o_l^N]$. By explicitly providing these object-specific tokens, the LLM can directly access the fine grained visual features of each anatomical object. This design allows \mathcal{LM} to directly reason over anatomical objects rather than implicitly inferring them from global image representations and then performing the task given in U . Finally, the \mathcal{LM} is trained for the next token prediction using Low-Rank Adaptation (LoRA) [12] and optimized with standard cross-entropy loss as shown in eq. 10.

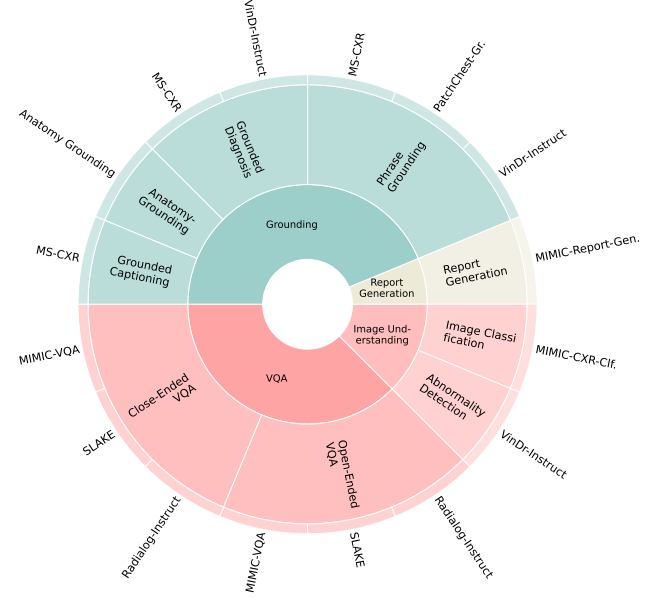


Figure 4. Set of 9 radiology tasks (middle circle) spanning 4 categories (inner circle) done by Anatomix and the datasets used (outer circle).

$$\mathcal{L}_{\mathcal{LM}} = -\frac{1}{T} \sum_{t=1}^T \sum_{w \in V} y_t(w) \log p_{\mathcal{LM}}(w | x_{<t}) \quad (10)$$

$$p_{\mathcal{LM}}(w | x_{<t}) = \text{Softmax}(\mathcal{LM}(x_{<t})) \quad (11)$$

where T is the total number of tokens in the sequence, V is the vocabulary, $x_{<t}$ represents the context tokens before position t , $y_t(w)$ is the one-hot ground truth distribution at step t , w denotes a token in the vocabulary V , and $p_{\mathcal{LM}}(w | x_{<t})$ is the probability assigned by \mathcal{LM} for token w given $x_{<t}$.

4. Experiments

4.1. Dataset

We train APM of Anatomix using more than 237,000 samples from the Chest ImaGenome [35] dataset, which extends MIMIC-CXR [14] with detailed spatial and semantic annotations, providing localized information for 36 anatomical objects and their observations. We used the given object-wise phrases for S_t and the given object bounding boxes for y_{box} prediction.

Supplementary Table S1 provides the summary of nine datasets used for \mathcal{LM} training. These datasets contain instruction-response pairs derived from eight publicly available CXR datasets including MIMIC-CXR-JPG [14], VinDr-CXR [26], MS-CXR [5], PadChest-Grounding [8],

Table 1. Performance on four grounding tasks. For Grounded Diagnosis (GD) and Grounded Captioning (GC), results are shown as GD / GC. AnatomXi- I_p and AnatomXi- \hat{O}_A represent the ablations discussed in section 6.

Model	NLG Metrics (GD / GC)			Clinical Metrics (GD / GC)		Phrase Grounding		Anatomy Grounding	
	BERTScore	ROUGE	METEOR	RadGraph-F1	CheXbert-14-F1	IoU	mAP	IoU	mAP
MAIRA-2	0.01 / 0.08	0.01 / 0.06	0.01 / 0.04	0.00 / 0.02	0.03 / 0.02	0.32	0.24	0.35	0.24
RadVLM	0.15 / 0.27	0.06 / 0.11	0.05 / 0.07	0.00 / 0.12	0.32 / 0.40	0.39	0.30	0.60	0.49
CheXagent	0.49 / 0.56	0.43 / 0.44	0.29 / 0.37	0.40 / 0.39	0.40 / 0.61	0.33	0.24	0.18	0.09
AnatomXi (ours)	0.63 / 0.65	0.60 / 0.56	0.42 / 0.48	0.58 / 0.50	0.54 / 0.78	0.46	0.35	0.73	0.66
AnatomXi- I_p	0.10 / 0.06	0.11 / 0.04	0.07 / 0.04	0.08 / 0.05	0.25 / 0.21	0.10	0.03	0.04	0.01
AnatomXi- \hat{O}_A	0.42 / 0.17	0.38 / 0.12	0.26 / 0.06	0.35 / 0.08	0.42 / 0.23	0.24	0.16	0.36	0.27

SLAKE [19], MIMIC-CXR-VQA [2], RaDialog-Instruct [27] and Chest-ImaGenome [35]. VinDr-Instruct, and Anatomy Grounding instruction-response datasets were created using the VinDr-CXR [26] and Chest ImaGenome [35] datasets, respectively.

4.2. Radiology Tasks

AnatomXi is trained on a diverse set of nine CXR-related tasks, spanning four categories: image understanding, grounding, report generation, and visual question answering (VQA), as illustrated in Fig. 4. The details of each task are provided in the supplementary material section S3.

4.3. Training Scheme

AnatomXi is trained in three steps that focus on different architectural components and tasks. The first step focuses on the end-to-end training of APM for anatomical object detection and contrastive alignment. We set the number of anatomical objects (N) = 36 and train APM for 45 epochs with 0.0001 learning rate. Followed by an alignment step (step 2), where we align the embedding space of \mathcal{LM} and APM by unfreezing the \mathcal{P}_{im} and \mathcal{P}_A projectors while keeping all other components frozen. This step uses the report generation dataset for 2 epoch training with 0.0002 learning. The third and final step focuses on instruction tuning, where we train \mathcal{LM} (using LoRA [12]) along with \mathcal{P}_{im} and \mathcal{P}_A for 4 epochs while keeping APM frozen. This step includes supervised fine-tuning on all nine tasks discussed in section 4.2. All training steps use AdamW [22] optimizer and were trained on 4 NVIDIA H100 GPUs with 80GB memory for approximately 125 hours.

5. Results and Discussion

5.1. Grounding

We begin by evaluating the model’s visual grounding capabilities. Specifically, we examine its ability to highlight relevant regions or pathologies on CXRs and to describe the features present within those regions. This information allows clinicians to visually verify the model’s pre-

dictions and gain insight into its decision making process. To assess these capabilities, we evaluate AnatomXi on four challenging grounding tasks using a combination of natural language generation (NLG), clinical, and detection metrics. We primarily compare our model against existing MLLMs with grounding capabilities, including RadVLM [10], Maira-2 [4], and CheXagent [7].

The phrase grounding and anatomy grounding tasks require localizing entities using bounding boxes. Accordingly, we evaluate these tasks using IoU and mean average precision (mAP) metrics. As shown in Table 1, AnatomXi significantly outperforms all other models by up to 15% in phrase grounding and over 25% in anatomy grounding. This substantial improvement stems from the anatomy-oriented design of AnatomXi, which enables the model to focus more effectively on specific anatomical structures. Fig. 5 illustrates representative samples of phrase and anatomy grounding tasks, where our model accurately localizes both anatomical regions and pathologies compared to the second best model RadVLM [10]. To further study the anatomical understanding, we perform phrase and anatomy grounding tasks on a flipped image as shown in Fig. 1. RadVLM [10] performs well on standard input but fails on flipped images, confusing left-right structures and relying on orientation cues. In contrast, AnatomXi preserves accurate grounding under flipping, demonstrating robust and spatially consistent anatomical reasoning—an essential capability for reliable medical image interpretation.

The grounded diagnosis and grounded captioning tasks, in contrast, require the model to identify pathologies or describe image content within a user-specified region. We evaluate performance on these tasks using both NLG (ROUGE [18], BERTScore [37], and METEOR [3]) and clinical (RadGraph-F1 [9] and CheXbert-14-F1 [32]) metrics. As shown in Table 1, AnatomXi consistently achieves the highest scores across all metrics providing upto 30% gains in grounded diagnosis and over 25 % improvement in grounded captioning tasks, further underscoring the effectiveness of its anatomy-aware architecture. Fig. 5 show sample input-outputs of AnatomXi and the second

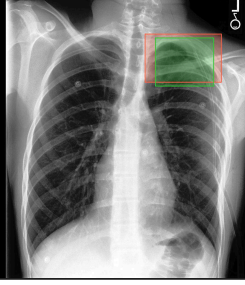
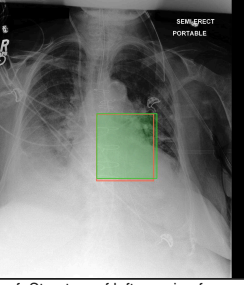
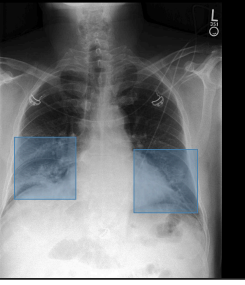
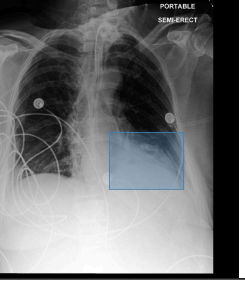
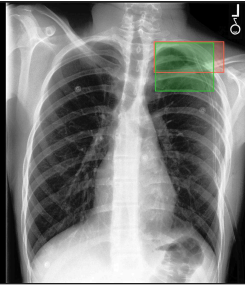
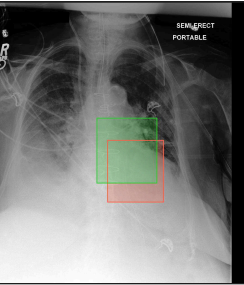
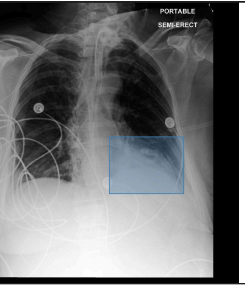
Task	Phrase Grounding	Anatomy Grounding	Grounded Captioning	Grounded Diagnosis
Prompt	Identify the position of the following finding in the CXR: small left pneumothorax	Where on this image is the Structure of left margin of heart located?	Describe the content of the following region(s): <box>(178,508),(403,735)</box><box>(612,552),(845,784)</box>	Please give the corresponding diagnosis for the following region(s): <box>(550,490),(823,699)</box>
AnatomiX (ours)				
	<ref>small left pneumothorax</ref><box>(560,133),(840,310)</box>	The <ref>Structure of left margin of heart</ref> is at <box>(451,422),(660,667)</box>	Bibasilar pneumonia	Pneumonia
RadVLM / CheXagent				
	This finding is located at [0.58, 0.14, 0.83, 0.25] in the image.	The location for the <ref>Structure of left margin of heart</ref> is marked at [0.48, 0.49, 0.68, 0.71] on the Chest X-ray.	bilateral lower lobe opacities	Pneumothorax
Ground Truth	<ref>small left pneumothorax</ref><box>(598,147),(812,324)</box>	For the <ref>Structure of left margin of heart</ref>, the coordinates are <box>(452,420),(672,658)</box> on the X-ray.	Bibasilar pneumonia	Pneumonia

Figure 5. Sample input–output pairs and comparison with second best models on grounding tasks. The upper panels show outputs from our model across four tasks. The lower panels compare AnatomiX with RadVLM [10] for phrase and anatomy grounding, and with CheXagent [7] for grounded diagnosis and captioning. Box colors: blue = user input, green = ground truth, red = model output.

best model CheXagent [7] for these two tasks, showcasing our model’s capacity to generate precise and clinically meaningful descriptions aligned with the specified regions. Notably, MAIRA-2 [4] model completely fails to perform these grounding tasks, as it was not trained to incorporate spatial or region-specific input.

5.2. Report Generation

The automatic generation of radiology reports is an important task that significantly reduces the time required for CXR interpretation and reporting. We evaluate this task using a set of NLG (ROUGE [18], BERTScore [37], METEOR [3]) and clinical (RadGraph-F1 [9], and CheXbert-14-F1 [32]) metrics. We compare our model against several SOTA CXR report generation models, including RadVLM [10], Maira-2 [4], CheXagent [7], Radialog [27], and Medgemma [30]. Table 2 shows that AnatomiX consistently outperforms competing approaches across metrics, demonstrating its strong capability in producing both linguistically coherent and clinically accurate reports. The

only exception occurs in CheXbert-14-F1 [32], where AnatomiX attains an F1 score of 0.42, compared to 0.48 for Radialog and 0.45 for Maira-2. Importantly, both of these models contain approximately $1.5 \times$ more parameters than AnatomiX, emphasizing the efficiency and scalability of our approach. These results collectively highlight AnatomiX’s balance between performance and computational efficiency, suggesting that it effectively captures domain-specific medical semantics without relying on excessively large model architectures.

5.3. Image Understanding

For the image understanding tasks, image classification and abnormality detection, we evaluate performance using AUROC, CheXbert-14-F1 [32], IoU, and mAP scores. AnatomiX outperforms all compared models in the image classification task and achieves the highest IoU for abnormality detection, while maintaining competitive mAP performance with leading approaches. The results in Table 3 highlight the model’s strong visual reasoning capabilities

Table 2. Report Generation performance grouped by NLG and Clinical metrics. AnatomiX- I_p and AnatomiX- \hat{O}_A represent the ablations.

Model	NLG Metrics			Clinical Metrics	
	ROUGE	BERTScore	METEOR	RadGraph	CheXbert-14 F1
MAIRA-2	0.43	0.25	0.12	0.17	0.45
Radialog	0.51	0.35	0.18	0.24	0.48
MedGamma	0.37	0.29	0.18	0.20	0.40
RadVLM	0.45	0.27	0.12	0.19	0.32
CheXagent	0.32	0.16	0.06	0.15	0.31
AnatomiX (ours)	0.53	0.38	0.21	0.26	0.42
AnatomiX- I_p	0.15	0.18	0.09	0.15	0.24
AnatomiX- \hat{O}_A	0.05	0.08	0.02	0.06	0.12

Table 3. Performance on image classification and abnormality detection tasks. AnatomiX- I_p and AnatomiX- \hat{O}_A represent ablations discussed in section 6.

Model	Image Classification (IC)		Abnormality Detection (AD)	
	AUROC	CheXbert-14-F1	IoU	mAP
MAIRA-2	0	0	0.16	0.01
Radialog	0.65	0.47	0	0
MedGamma	0.58	0.40	0.04	0
RadVLM	0.63	0.43	0.28	0.12
CheXagent	0.92	0.85	0.31	0.22
AnatomiX (ours)	0.92	0.85	0.31	0.20
AnatomiX- I_p	0.85	0.75	0.08	0.06
AnatomiX- \hat{O}_A	0.88	0.77	0.15	0.10

and reliable localization performance.

5.4. Visual Question Answering (VQA)

We benchmark AnatomiX on both open- and close-ended VQA tasks using BERTScore [37] and CheXbert-14-F1 [32]. AnatomiX demonstrates strong performance across both settings (Table 4), outperforming all models and matching or exceeding CheXagent [7]. Minor score differences mainly arise from keywords mismatch with the ground truth, for example when the ground truth for the question “*Is there any pneumonia in the image?*” is “yes, *pneumonia is present*” but the model outputs only “yes”, or vice versa, these metrics assign a lower score despite both being clinically correct. Overall, these results highlight AnatomiX’s high VQA capabilities.

6. Ablation

LLM: We conduct two ablations to analyze the effect of anatomical and textual inputs. In AnatomiX- I_p , only image embeddings I_p are provided to \mathcal{LM} , excluding anatomical tokens, bounding boxes, and retrieved sentences. In AnatomiX- \hat{O}_A , we add \hat{O}_A alongside I_p to isolate the influence of y_{box} and \hat{S}_t . As shown in Table 1, removing anatomical information causes a major performance drop, while adding \hat{O}_A partially recovers results but remains limited on grounded captioning, which requires detailed de-

Table 4. Open and close ended VQA task performance. AnatomiX- I_p and AnatomiX- \hat{O}_A represent ablation experiments.

Model	Open-Ended VQA		Close-Ended VQA	
	BERTScore	CheXbert-14 F1	BERTScore	CheXbert-14 F1
MAIRA-2	0.07	0.31	0.10	0.81
Radialog	0.08	0.43	0.03	0.92
MedGemma	0.03	0.44	0.02	0.38
RadVLM	0.07	0.04	0.23	0.67
CheXagent	0.86	0.87	0.90	0.97
AnatomiX (ours)	0.86	0.86	0.89	0.95
AnatomiX- I_p	0.38	0.64	0.61	0.87
AnatomiX- \hat{O}_A	0.39	0.52	0.48	0.79

Table 5. Ablation experiments for APM. AnatomiX-wo- \mathcal{M} represents experiment without \mathcal{M} while AnatomiX-Dino shows the experiment with DinoV3 as image encoder.

Model	y_{box} Metrics		\hat{S}_t Metrics		
	IoU	CheXbert-14-F1	RadGraph-F1	METEOR	
AnatomiX-wo- \mathcal{M}	0.781	0.627	0.689	0.71	
AnatomiX-Dino	0.792	0.614	0.673	0.694	
AnatomiX	0.812	0.634	0.709	0.727	

scriptions. For report generation (Table 2), including \hat{O}_A without retrieved sentences reduces performance, indicating that \hat{S}_t is essential for descriptive tasks. Similar trends in VQA and image understanding (Tables 3 and 4) suggest that \hat{O}_A aids spatial reasoning, whereas \hat{S}_t primarily benefits linguistically rich tasks.

APM: We conduct two ablations to assess the architectural components of APM. First, we replace the image encoder \mathcal{E} with a pretrained DinoV3 encoder [31], referred to as AnatomiX-Dino. Second, we evaluate the role of \mathcal{M} by performing contrastive alignment directly using the output of the decoder \mathcal{D} and removing \mathcal{M} , denoted as AnatomiX-wo- \mathcal{M} . For object detection (y_{box} prediction), we report IoU, and for contrastive retrieval, we report CheXbert-14-F1 [32], RadGraph-F1 [9], and METEOR [3] scores by comparing the retrieved text \hat{S}_t with ground truth sentences. As shown in Table 5, DinoV3 yields competitive IoU but lower textual correctness, while removing \mathcal{M} leads to an overall performance drop—indicating that \mathcal{M} enhances anatomical feature extraction and improves sentence retrieval.

7. Conclusion

In conclusion, AnatomiX shows significant improvements in CXR interpretation, especially in tasks that require a direct anatomical understanding. Our results highlight that anatomy-oriented design is the key to accurate spatial reasoning in medical MLLMs. While finetuning natural image MLLMs on large medical datasets can help, it can create false spatial correspondences. Future work could extend anatomy oriented architectures to other modalities such as

MRI and echocardiography. This study focuses on single turn interactions; extending it to multi turn setups would enhance flexibility and applicability. Overall, this work marks an important step toward domain-specific design in MLLMs.

References

- [1] DM Anisuzzaman, Jeffrey G Malins, Paul A Friedman, and Zachi I Attia. Fine-tuning llms for specialized use cases. *Mayo Clinic Proceedings: Digital Health*, 2024. [1](#)
- [2] Seongsu Bae, Daeun Kyung, Jaehee Ryu, Eunbyeol Cho, Gyubok Lee, Sunjun Kweon, Jungwoo Oh, Lei Ji, Eric Chang, Tackeun Kim, et al. Mimic-ext-mimic-cxr-vqa: A complex, diverse, and large-scale visual question answering dataset for chest x-ray images, 2024. [6](#)
- [3] Satanjeev Banerjee and Alon Lavie. Meteor: An automatic metric for mt evaluation with improved correlation with human judgments. In *Proceedings of the acl workshop on intrinsic and extrinsic evaluation measures for machine translation and/or summarization*, pages 65–72, 2005. [6, 7, 8](#)
- [4] Shruthi Bannur, Kenza Bouzid, Daniel C Castro, Anton Schwaighofer, Anja Thieme, Sam Bond-Taylor, Maximilian Ilse, Fernando Pérez-García, Valentina Salvatelli, Harshita Sharma, et al. Maira-2: Grounded radiology report generation. *arXiv preprint arXiv:2406.04449*, 2024. [1, 2, 6, 7](#)
- [5] Benedikt Boecking, Naoto Usuyama, Shruthi Bannur, Daniel C Castro, Anton Schwaighofer, Stephanie Hyland, Maria Wetscherek, Tristan Naumann, Aditya Nori, Javier Alvarez-Valle, et al. Making the most of text semantics to improve biomedical vision–language processing. In *European conference on computer vision*, pages 1–21. Springer, 2022. [5](#)
- [6] Nicolas Carion, Francisco Massa, Gabriel Synnaeve, Nicolas Usunier, Alexander Kirillov, and Sergey Zagoruyko. End-to-end object detection with transformers. In *European conference on computer vision*, pages 213–229. Springer, 2020. [3](#)
- [7] Zhihong Chen, Maya Varma, Jean-Benoit Delbrouck, Magdalini Paschali, Louis Blankemeier, Dave Van Veen, Jeya Maria Jose Valanarasu, Alaa Youssef, Joseph Paul Cohen, Eduardo Pontes Reis, et al. Chexagent: Towards a foundation model for chest x-ray interpretation. *arXiv preprint arXiv:2401.12208*, 2024. [1, 2, 6, 7, 8](#)
- [8] Daniel Coelho de Castro, Aurelia Bustos, Shruthi Bannur, Stephanie L Hyland, Kenza Bouzid, Maria Teodora Wetscherek, Maria Dolores Sánchez-Valverde, Lara Jaques-Pérez, Lourdes Pérez-Rodríguez, Kenji Takeda, et al. Padchest-gr: A bilingual chest x-ray dataset for grounded radiology report generation. *NEJM AI*, 2(7):AIdbp2401120, 2025. [5](#)
- [9] Jean-Benoit Delbrouck, Pierre Chambon, Christian Bluethgen, Emily Tsai, Omar Almusa, and Curtis P Langlotz. Improving the factual correctness of radiology report generation with semantic rewards. *arXiv preprint arXiv:2210.12186*, 2022. [6, 7, 8](#)
- [10] Nicolas Deperrois, Hidetoshi Matsuo, Samuel Ruipérez-Campillo, Moritz Vandenhirtz, Sonia Laguna, Alain Ryser, Koji Fujimoto, Mizuho Nishio, Thomas M Sutter, Julia E Vogt, et al. Radvlm: A multitask conversational vision-language model for radiology. *arXiv preprint arXiv:2502.03333*, 2025. [1, 2, 6, 7](#)
- [11] Yu Gu, Robert Tinn, Hao Cheng, Michael Lucas, Naoto Usuyama, Xiaodong Liu, Tristan Naumann, Jianfeng Gao, and Hoifung Poon. Domain-specific language model pre-training for biomedical natural language processing. *ACM Transactions on Computing for Healthcare (HEALTH)*, 3(1):1–23, 2021. [4](#)
- [12] Edward J Hu, Yelong Shen, Phillip Wallis, Zeyuan Allen-Zhu, Yuanzhi Li, Shean Wang, Lu Wang, Weizhu Chen, et al. Lora: Low-rank adaptation of large language models. *ICLR*, 1(2):3, 2022. [5, 6](#)
- [13] Ding Jiang and Mang Ye. Cross-modal implicit relation reasoning and aligning for text-to-image person retrieval. In *Proceedings of the IEEE/CVF conference on computer vision and pattern recognition*, pages 2787–2797, 2023. [4](#)
- [14] Alistair EW Johnson, Tom J Pollard, Seth J Berkowitz, Nathaniel R Greenbaum, Matthew P Lungren, Chih-ying Deng, Roger G Mark, and Steven Horng. Mimic-cxr, a de-identified publicly available database of chest radiographs with free-text reports. *Scientific data*, 6(1):317, 2019. [5](#)
- [15] Alexander Kirillov, Eric Mintun, Nikhila Ravi, Hanzi Mao, Chloe Rolland, Laura Gustafson, Tete Xiao, Spencer Whitehead, Alexander C Berg, Wan-Yen Lo, et al. Segment anything. In *Proceedings of the IEEE/CVF international conference on computer vision*, pages 4015–4026, 2023. [2](#)
- [16] Chunyuan Li, Cliff Wong, Sheng Zhang, Naoto Usuyama, Haotian Liu, Jianwei Yang, Tristan Naumann, Hoifung Poon, and Jianfeng Gao. Llava-med: Training a large language-and-vision assistant for biomedicine in one day. *Advances in Neural Information Processing Systems*, 36:28541–28564, 2023. [2](#)
- [17] Qingqiu Li, Zihang Cui, Seongsu Bae, Jilan Xu, Runtian Yuan, Yuejie Zhang, Rui Feng, Quanli Shen, Xiaobo Zhang, Junjun He, et al. Aor: Anatomical ontology-guided reasoning for medical large multimodal model in chest x-ray interpretation. *arXiv preprint arXiv:2505.02830*, 2025. [2](#)
- [18] Chin-Yew Lin. Rouge: A package for automatic evaluation of summaries. In *Text summarization branches out*, pages 74–81, 2004. [6, 7](#)
- [19] Bo Liu, Li-Ming Zhan, Li Xu, Lin Ma, Yan Yang, and Xiao-Ming Wu. Slake: A semantically-labeled knowledge-enhanced dataset for medical visual question answering. In *2021 IEEE 18th international symposium on biomedical imaging (ISBI)*, pages 1650–1654. IEEE, 2021. [6](#)
- [20] Haotian Liu, Chunyuan Li, Qingyang Wu, and Yong Jae Lee. Visual instruction tuning. *Advances in neural information processing systems*, 36:34892–34916, 2023. [1, 2](#)
- [21] Jingping Liu, Ziyuan Liu, Zhedong Cen, Yan Zhou, Yinan Zou, Weiyan Zhang, Haiyun Jiang, and Tong Ruan. Can multimodal large language models understand spatial relations? *arXiv preprint arXiv:2505.19015*, 2025. [1](#)
- [22] Ilya Loshchilov and Frank Hutter. Decoupled weight decay regularization. *arXiv preprint arXiv:1711.05101*, 2017. [6](#)
- [23] Lingxiao Luo, Bingda Tang, Xuanzhong Chen, Rong Han, and Ting Chen. Vividmed: Vision language model with

versatile visual grounding for medicine. *arXiv preprint arXiv:2410.12694*, 2024. 1, 2

[24] Chuofan Ma, Yi Jiang, Jiannan Wu, Zehuan Yuan, and Xiaojuan Qi. Groma: Localized visual tokenization for grounding multimodal large language models. In *European Conference on Computer Vision*, pages 417–435. Springer, 2024. 1

[25] Philip Müller, Georgios Kaassis, and Daniel Rueckert. Chex: Interactive localization and region description in chest x-rays. In *European Conference on Computer Vision*, pages 92–111. Springer, 2024. 2

[26] Ha Q Nguyen, Khanh Lam, Linh T Le, Hieu H Pham, Dat Q Tran, Dung B Nguyen, Dung D Le, Chi M Pham, Hang TT Tong, Diep H Dinh, et al. Vindr-cxr: An open dataset of chest x-rays with radiologist’s annotations. *Scientific Data*, 9(1):429, 2022. 5, 6

[27] Chantal Pellegrini, Ege Özsoy, Benjamin Busam, Nassir Navab, and Matthias Keicher. Radialog instruct dataset. 2, 6, 7

[28] Zhiliang Peng, Wenhui Wang, Li Dong, Yaru Hao, Shaohan Huang, Shuming Ma, and Furu Wei. Kosmos-2: Grounding multimodal large language models to the world. *arXiv preprint arXiv:2306.14824*, 2023. 1

[29] Alec Radford, Jong Wook Kim, Chris Hallacy, Aditya Ramesh, Gabriel Goh, Sandhini Agarwal, Girish Sastry, Amanda Askell, Pamela Mishkin, Jack Clark, et al. Learning transferable visual models from natural language supervision. In *International conference on machine learning*, pages 8748–8763. PMLR, 2021. 4

[30] Andrew Sellergren, Sahar Kazemzadeh, Tiam Jaroensri, Atilla Kiraly, Madeleine Traverse, Timo Kohlberger, Shawn Xu, Fayaz Jamil, Cian Hughes, Charles Lau, et al. Medgemma technical report. *arXiv preprint arXiv:2507.05201*, 2025. 2, 5, 7

[31] Oriane Siméoni, Huy V Vo, Maximilian Seitzer, Federico Baldassarre, Maxime Oquab, Cijo Jose, Vasil Khalidov, Marc Szafraniec, Seungeun Yi, Michaël Ramamonjisoa, et al. Dinov3. *arXiv preprint arXiv:2508.10104*, 2025. 8

[32] Akshay Smit, Saahil Jain, Pranav Rajpurkar, Anuj Pareek, Andrew Y Ng, and Matthew P Lungren. Chexbert: combining automatic labelers and expert annotations for accurate radiology report labeling using bert. *arXiv preprint arXiv:2004.09167*, 2020. 6, 7, 8

[33] Andrew Szot, Bogdan Mazoure, Harsh Agrawal, R Devon Hjelm, Zsolt Kira, and Alexander Toshev. Grounding multimodal large language models in actions. *Advances in Neural Information Processing Systems*, 37:20198–20224, 2024. 1

[34] Daniel Wolf, Heiko Hillenagen, Billurvan Taskin, Alex Bäuerle, Meinrad Beer, Michael Götz, and Timo Ropinski. Your other left! vision-language models fail to identify relative positions in medical images. In *International Conference on Medical Image Computing and Computer-Assisted Intervention*, pages 691–701. Springer, 2025. 1, 3

[35] Joy T Wu, Nkechinyere N Agu, Ismini Lourentzou, Arjun Sharma, Joseph A Paguio, Jasper S Yao, Edward C Dee, William Mitchell, Satyananda Kashyap, Andrea Giovannini, et al. Chest imangenome dataset for clinical reasoning. *arXiv preprint arXiv:2108.00316*, 2021. 5, 6

[36] Hanguang Xiao, Feizhong Zhou, Xingyue Liu, Tianqi Liu, Zhipeng Li, Xin Liu, and Xiaoxuan Huang. A comprehensive survey of large language models and multimodal large language models in medicine. *Information Fusion*, page 102888, 2024. 1

[37] Tianyi Zhang, Varsha Kishore, Felix Wu, Kilian Q Weinberger, and Yoav Artzi. Bertscore: Evaluating text generation with bert. *arXiv preprint arXiv:1904.09675*, 2019. 6, 7, 8

[38] Ke Zou, Yang Bai, Zhihao Chen, Yang Zhou, Yidi Chen, Kai Ren, Meng Wang, Xuedong Yuan, Xiaojing Shen, and Huazhu Fu. Medrg: Medical report grounding with multi-modal large language model. *arXiv preprint arXiv:2404.06798*, 2024. 2

AnatomiX, an Anatomy-Aware Grounded Multimodal Large Language Model for Chest X-Ray Interpretation

Supplementary Material

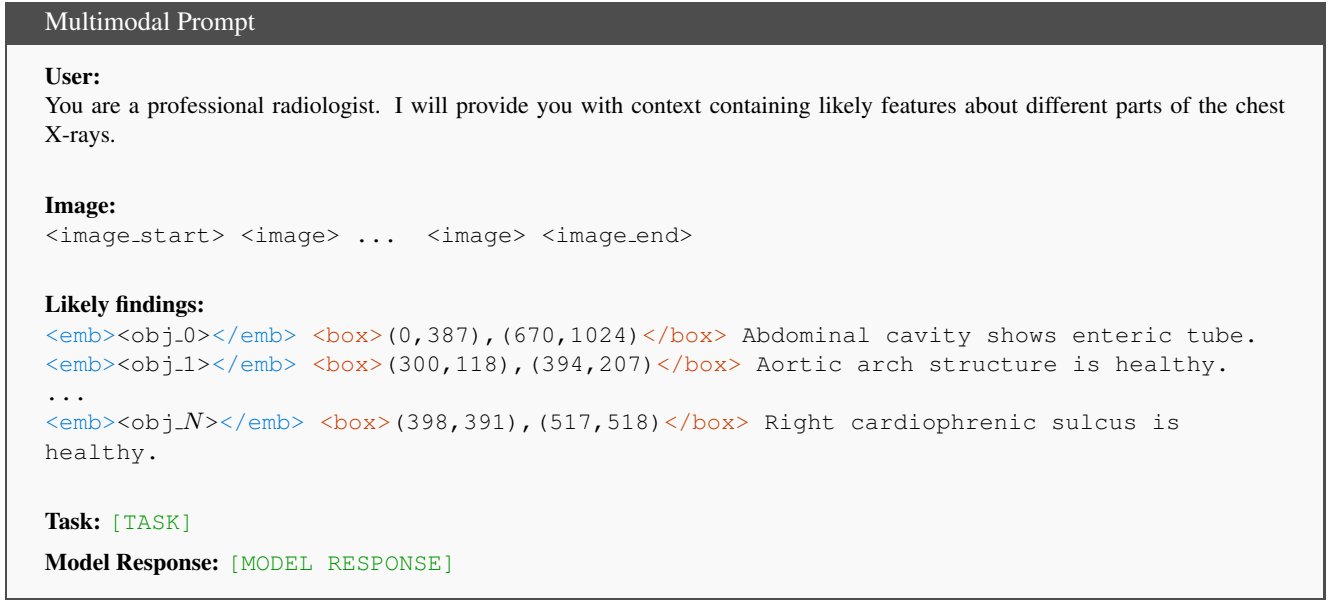


Figure S1. Multimodal prompt template used in \mathcal{LM} . Colored tags ($<\text{emb}>$ and $<\text{box}>$) denote special tokens corresponding to anatomical object embeddings and bounding boxes, respectively. Each $<\text{obj}_i>$ token represents the embedding of the i^{th} anatomical object, while $<\text{image}>$ indicates image patch embeddings.

S1. Self-Similarity Loss Matrix

The Contrastive Alignment stage of the Anatomy Perception Module (APM) utilizes the Self-Similarity matrix \mathbf{S}_{self} to model fine grained semantic relations among anatomical descriptions. In this stage, a pretrained sentence encoder \mathcal{S} provides indirect supervision by embedding textual inputs into a continuous semantic space that captures linguistic and clinical similarities. Given a set of input sentences S_t , each sentence is encoded through \mathcal{S} to obtain text embeddings $\mathbf{S}_E \in \mathbb{R}^{N \times 768}$, where each row corresponds to the representation of one sentence in a 768-dimensional embedding space. To ensure consistency and comparability across representations, the embeddings are first normalized using ℓ_2 normalization:

$$\bar{\mathbf{S}}_E = \frac{\mathbf{S}_E}{|\mathbf{S}_E|_2} \quad (\text{S1})$$

This normalization projects the embeddings onto a unit hypersphere, ensuring that they encode directional (semantic) differences rather than magnitude based variations. The normalized embeddings are then used to compute the Self-Similarity matrix:

$$\mathbf{S}_{self} = \text{Softmax}(\bar{\mathbf{S}}_E) \cdot \text{Softmax}(\bar{\mathbf{S}}_E)^T \quad (\text{S2})$$

where $\mathbf{S}_{self} \in \mathbb{R}^{N \times N}$ encodes pairwise similarity scores between all sentences in S_t . The softmax operation (applied row wise) ensures these similarities are smooth and probabilistically interpretable.

Next, to align anatomical and textual semantics, we compute a projected similarity matrix $\hat{\mathbf{K}}_A$ between the projected anatomical features $\hat{\mathbf{O}}_A$ and projected text embeddings $\hat{\mathbf{S}}_A$:

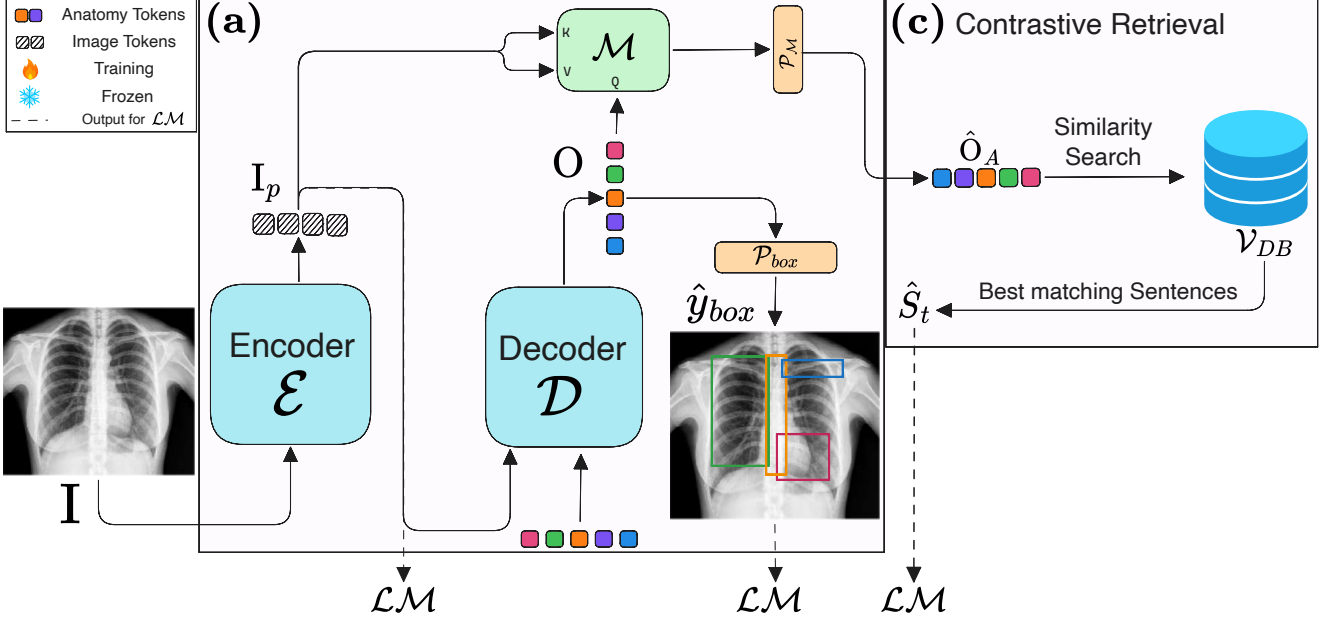


Figure S2. APM architecture during inference, where the Contrastive Alignment’s components are replaced with vector database for the Contrastive Retrieval. See Fig. 2 for training architecture.

$$\hat{\mathbf{K}}_A = \text{Softmax} \left(\frac{\hat{\mathbf{O}}_A \hat{\mathbf{S}}_A^T}{\tau} \right) \quad (S3)$$

where $\hat{\mathbf{K}}_A \in \mathbb{R}^{N \times N}$, and τ is the temperature coefficient (set to 0.01) that controls the sharpness of the similarity distribution.

The final contrastive alignment loss is defined as the averaged KL-divergence between the anatomical–textual similarity matrix $\hat{\mathbf{K}}_A$ and the self-similarity matrix \mathbf{S}_{self} , computed in both row-wise and column-wise directions to enforce mutual consistency:

$$\mathcal{L}_{CL} = \frac{1}{2} KL \left(\hat{\mathbf{K}}_A, \mathbf{S}_{self} \right) + \frac{1}{2} KL \left(\hat{\mathbf{K}}_A^T, \mathbf{S}_{self}^T \right) \quad (S4)$$

This formulation encourages $\hat{\mathbf{O}}_A$ and $\hat{\mathbf{S}}_A$ to maintain pairwise relationships that reflect the semantic structure captured in \mathbf{S}_{self} . As a result, the APM preserves semantic coherence and clinical consistency across related sentences, capturing overlapping anatomical features rather than enforcing strict one-to-one alignments.

S2. Vector Database

During APM inference, we replace the Contrastive Alignment with the Contrastive Retrieval (see Fig. S2) to identify the semantically most similar sentences to the anatomical object tokens $\hat{\mathbf{O}}_A$. These retrieved sentences represent the most probable observations for each anatomical object and thus provide important contextual information for downstream descriptive tasks in \mathcal{LM} , as discussed in ablations.

The vector database, denoted as \mathcal{V}_{DB} , stores all unique sentences associated with each anatomical object from the validation set of the Chest-ImaGenome dataset. For every object in an image, we construct a concise descriptive sentence using the corresponding phrases and attributes given in the original dataset (example sentence: “Right lower lung shows pleural effusion and atelectasis”). To build \mathcal{V}_{DB} , we first compile the set of unique sentences for each anatomical object. Each sentence is then encoded using the sentence encoder \mathcal{S} and the trained projection head \mathcal{P}_S , producing s -dimensional embeddings (see Fig. 2 for \mathcal{P}_S). These embeddings, along with their corresponding sentences, are stored as key–value pairs in \mathcal{V}_{DB} , with a distinct sub-database allocated to each anatomical object. Consequently, \mathcal{V}_{DB} comprises N independent sub-databases.

The compact nature of both the embeddings and the sentences ensures that \mathcal{V}_{DB} remains lightweight, enabling efficient retrieval at inference time. During inference, a similarity search is performed between each anatomical object token $\hat{\mathbf{O}}_A$

Table S1. Number of training, validation, and test samples for the nine datasets used in \mathcal{LM} training and validation. The “Source” column indicates the original public dataset used directly or as the basis for dataset creation.

Dataset	Source	Test	Train	Val
MIMIC-VQA	MIMIC-CXR-VQA	5,497	101,963	4,926
RaDialog Instruct	RaDialog Instruct	799	6,274	822
SLAKE	SLAKE	298	1,175	285
Anatomy Grounding	Chest-ImaGenome	3,403	237,938	1,959
MS-CXR	MS-CXR	528	2,445	507
VinDr-Instruct	VinDr-CXR	6,166	38,122	4,099
PadChest-Grounding	PadChest-Grounding	1,121	3,920	558
MIMIC-CXR Classification	MIMIC-CXR	2,957	182,425	1,666
MIMIC Report Gen	MIMIC-CXR	1,722	135,049	1,078
Total	-	22,491	709,311	15,900

and the sentence embeddings within the corresponding sub-database of \mathcal{V}_{DB} , thereby retrieving the most relevant descriptive sentences for each object. These sentences are then passed to \mathcal{LM} using a multimodal prompt template shown in Fig. S1, where they provide important contextual information about each anatomy.

S3. Radiology Tasks

AnatomiX is trained and evaluated on nine CXR-related tasks, spanning four categories: image understanding, grounding, report generation, and visual question answering (VQA). Each of these tasks is focused on specific aspect of the CXR interpretation and uses different dataset(s).

S3.1. Image Understanding

This category includes multi-label image classification across 14 classes using the MIMIC-CXR dataset, as well as CXR abnormality detection leveraging the VinDr-Instruct dataset. Fig. S4 shows sample input-output samples for classification and abnormality detection tasks along with the output of our model.

S3.2. Grounding

We include four challenging grounding tasks in this work, namely: Phrase Grounding, Grounded Diagnosis, Grounded Captioning, and Anatomy Grounding. In Phrase Grounding, the model identifies the spatial location of a given phrase within an input image, utilizing the MS-CXR, PadChest-Gr, and VinDr-Instruct datasets. Grounded Diagnosis and Grounded Captioning require the model to infer a diagnosis and generate a textual description for a specified image region, respectively; we use VinDr-Instruct and MS-CXR for Grounded Diagnosis and MS-CXR for Grounded Captioning. Finally, Anatomy Grounding uses the Anatomy-Grounding dataset to localize anatomical structures based on user-provided textual prompts. Fig. 5 shows sample input and output pairs for these tasks, along with the output of our model.

S3.3. Report Generation

This task involves generating the full report, including both the findings and impression sections using MIMIC-CXR dataset. A sample image-report is shown in Fig. S3 along with the output of AnatomiX.

S3.4. Visual Question Answering

The VQA category consists of open-ended and closed-ended question answering tasks, derived from a combination of the MIMIC-VQA, SLAKE, and Radialog-Instruct datasets.

Write a comprehensive report:

Findings:
The patient is status post median sternotomy and CABG. Left-sided AICD/pacemaker device is noted with leads terminating in the right atrium and right ventricle. Heart size remains mildly enlarged. Mediastinal and hilar contours are unchanged. There is mild pulmonary vascular congestion. Patchy opacities in the lung bases may reflect atelectasis. No pleural effusion or pneumothorax is present. There are no acute osseous abnormalities.

Impression:
Mild pulmonary vascular congestion and bibasilar atelectasis.

Findings:
Left-sided pacer is re- demonstrated with leads terminating in the right atrium and right ventricle. The patient is status post median sternotomy, aortic valve replacement, and CABG. Heart size is mildly enlarged, unchanged. Mediastinal and hilar contours are similar. Mild upper zone pulmonary vascular redistribution is likely chronic without overt pulmonary edema. Lung volumes remain low with streaky opacities in the lung bases suggestive of atelectasis. No large pleural effusion or pneumothorax is present. Fusion hardware within the lumbar spine is partially imaged as well as hardware within the right humeral head.

Impression:
Chronic mild pulmonary vascular congestion without overt pulmonary edema. Bibasilar atelectasis.

Figure S3. Sample report generation task. Color scheme: Blue color for user input prompt, red shows the report generated by AnatomiX, and green represents the ground truth report.

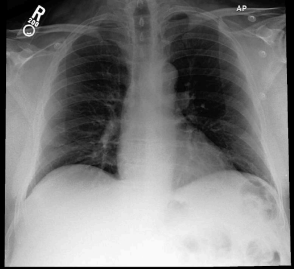
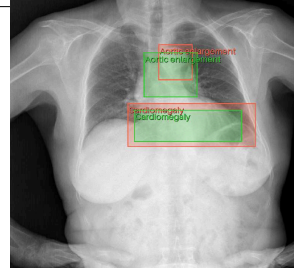
Open-Ended VQA	Close-Ended VQA	Abnormality Detection	Image Classification
		 <p>Locate areas in the chest X-ray where abnormalities are present, using bounding box coordinates</p> <p>Cardiomegaly (399,455), (835,605) Aortic enlargement (504,252), (620,375)</p>	 <p>Given the CXR, identify any diseases. Options:</p> <p>(c) Lung Lesion (v) No Finding (p) Pleural Effusion (a) Support Devices (r) Edema (x) Pneumothorax (c) Atelectasis (n) Enlarged Cardiomediastinum (j) Pleural Other (k) Pneumonia (w) Lung Opacity (q) Fracture (u) Consolidation (l) Cardiomegaly There may be more than one answer.</p> <p>(p) Pleural Effusion, (c) Atelectasis (p) Pleural Effusion, (c) Atelectasis</p>
What are the key observations derived from this chest x-ray?	Does the image show pneumothorax?		
The patient has lung opacity, atelectasis and pleural effusion.	No, there is no evidence of that in the image.		
Sure, atelectasis and pleural effusion.	No, there is not.		

Figure S4. Example input-output-ground truth for image understanding and visual question answering tasks. User input prompt is shown in blue color, red color represents AnatomiX's output, while ground truth is shown in green.